International Journal of Science and Research Archive

eISSN: 2582-8185

Cross Ref DOI: 10.30574/ijsra

Journal homepage: https://ijsra.net/

(RESEARCH ARTICLE)

Check for updates

Numerical investigation of Martian blades using various Airfoils

Abdur Rahman, Ndouba Ange Benai-dara *, Caijun Xue and Leon Kaswango Kanama

College of Aerospace Engineering Nanjing University of Aeronautics and Astronautics, Nanjing 210016, China.

International Journal of Science and Research Archive, 2024, 13(02), 3269-3278

Publication history: Received on 12 November 2024; revised on 21 December 2024; accepted on 23 December 2024

Article DOI: https://doi.org/10.30574/ijsra.2024.13.2.2564

Abstract

Due to the low Reynolds number compressible regime of the Martian atmosphere, the airfoil utilized to design the blade is of significant importance. The current study aims at evaluating the 2D performance of NACA 5605, Camber 4603 and DEP 4535-01 airfoils and the hovering performance of the blades built with these three airfoils using numerical analysis. The result has revealed that the type of airfoil for the blade design depends on the pitch angle at which the Figure of Merit reaches its peak. Prior to that pitch angle, which is 8deg, DEP 4535-01 airfoil is beneficial otherwise NACA 5605 is desirable. At the pitch angle of 8deg, the Figure of Merit of DEP 4535-01, NACA 5605 and Camber 4603 blades are 0.73, 0.71 and 0.70 respectively. Finally, the structural analysis is conducted on DEP 4535-01 blade to ensure the thickness distribution. The maximum stress and deformation are 393.15MPa and 485.54mm respectively and the minimum factory of safety is 1.12, which indicates the need of internal structures for the blade.

Keywords: Airfoils; Martian blade design; Numerical analysis; Figure of merit; Structure analysis

1. Introduction

The Martian atmosphere is characterized by a low density ($\rho = 0.0178 kg/m^3$) and low speed of sound ($a = 233 m/s$) which result in low Reynolds number compressible regime [1]-[3]. This regime combines the effects of low Reynolds number and high Mach number, two phenomena affecting the airfoil and blade performance. At low Reynolds number flow, the boundary layer does not carry sufficient momentum and as a result, the shear layer separates when encountering a strong adverse pressure gradient. The separated shear layer can act like a boundary layer trip incepting Kelvin-Helmholtz vortices which break down into small turbulent spots resulting in reattachment. The length between the boundary layer separation and reattachment known as Laminar Separation Bubble LSB reduces the effective camber and increases the pressure drag. Added to the low Reynolds number phenomenon is the compressible effect which results in shock wave formation. These two phenomena require a careful selection of the airfoil to design a high-performance blade.

The blade structure is composed of cross-section airfoils which vary in shape (thickness and camber distribution and chord length) and twist angle along the blade radius thus, the blade performance depends on the aerodynamic characteristics of the airfoils. Koning et al. [4]-[6] surveyed the airfoils to be employed for the blade design at Martian atmospheric conditions and concluded that cambered, thin and sharp edge airfoils are beneficial as they help delay the boundary layer separation and reattachment points. The optimized airfoils for Martian micro rotorcraft obtained by Désert et al. [7] and Oyama et Fujii [8] are cambered from leading to trailing edge. The rotor blade of Mars Helicopter Ingenuity, which operation on the planet ended in the beginning of 2024 was designed using CLF 5605 airfoil. The airfoil was optimized to generate high lift-to-drag ratio as well as to meet the structural requirement. However, as revealed recently by Koning et al. [9], the primary source of stress for a Martian blade is the inertia force rather than aerodynamic load and the thickness of CLF 5605 airfoil can be reduced further to increase the overall performance. Monday et al. [10] investigated the performance of a sharp edge triangular airfoil and found the airfoil to exhibit high non-linear lift at high

* Corresponding author: Ndouba Ange Benai-dara

angles of attack due to the vortex generated by the sharp leading edge. Many more of these studies are limited to 2D and there are few researchers who have ventured to evaluate the aerodynamic performance of the blade design using various airfoil categories. The current study is conducted to fill this gap by using three categories of airfoils to know, NACA 5605, Camber 4603 and Double-edged plat DEP 4535-01 as shown in Figure 1.

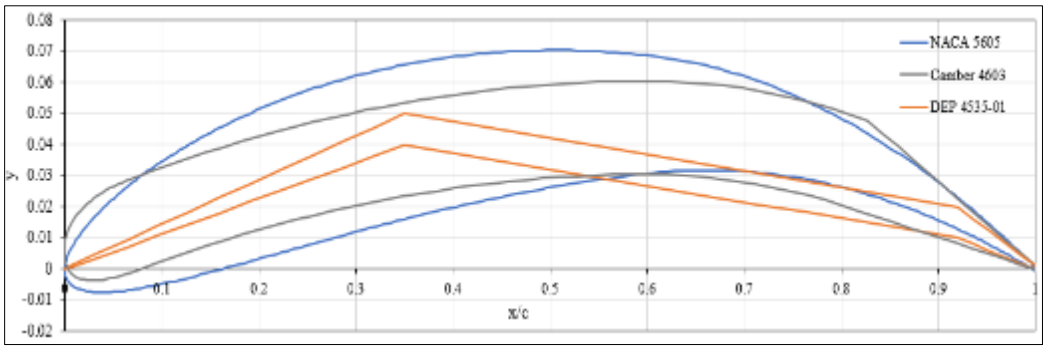

Figure 1 Three airfoils used to design the three Martian blades.

With the advent in super power computers, Computational Fluid Dynamics CFD and Finite Element Analysis FEA offer possibilities to accurately predict the low Reynolds number compressible flow regime over a blade including root, spanwise and tip effects and to perform structural analysis provided the solver has adequate resolution. Marinus et al. [11] and Mian et al. [12] compared the blade aerodynamic results obtained by low-fidelity and CFD and found that CFD results agreed well with the experimental data. Brocklehurst et Barakos [13] employed the high-resolution CFD to gain deeper insight into blade aerodynamics and tip design. Among the adequate resolution the CFD solver needs to have, is the selection of a model. The most reliable models such as Direct Numerical Simulation DNS and Large Eddy Simulation LES are costly especially when computing for blade aerodynamics that requires over millions of elements to capture the tip effect. Koning et al. [14] evaluated the performance of a transition model with that of fully turbulent model in predicting the Figure of Merit FM of Ingenuity rotor. The transition model prediction agreed well with the experimental curve even after the peak FM whereas fully turbulent model overpredicts the efficiency metric. Thus, the transition model $SST\ \gamma - Re_\theta$, coupling the equations of the shear stress transport, intermittency γ and thickness momentum Reynolds number is utilized. The model does not rely on nonlocal parameters which make it suitable for CFD codes and complicated predictions [15-16]. CFD results can be coupled with the Finite Element Method to account for the natural frequencies, blade deformations, root loads and 3D stresses resulting in Fluid-Structure Interaction FSI.

The current paper aims at investigating the airfoil aerodynamic efficiency of the three airfoils (NACA 5605, Camber 4603 and DEP 4535-01) and the hovering performance of the three blades using CFD solver, Fluent. The 2D performance of the airfoils is evaluated at 75% of the blade radius where the Mach and Reynolds numbers are 0.56 and 18692 respectively. As for the blade, the design constraints are the blade radius being 0.6m, a payload of 1.8kg and the tip Mach number of 0.75 equivalent to 2783RPM. The projected area of the blades is approximately equal to that of Lumba et al. [17] and the pitch axis is at 40% chord. To ensure the structure safety of DEP 4535-01 blade, the finite element analysis is conducted by using Carbon Fiber as material and applying the pressure contour obtained from CFD solver and the inertia force.

2. Rotor Reynolds number and hovering performance

Reynolds number is generally given as the ratio of inertial force to viscous force where the reference length is the length of the object being studied. However, when a rotor blade is considered, the reference length is the chord length at 75% of the blade radius and Reynolds number is given as:

$$Re = \frac{\rho V_{wake} C_{0.75R}}{\mu} = \frac{\rho(0.75\Omega R) C_{0.75R}}{\mu}. \quad \text{.....(1)}$$

Where ρ and μ are the fluid density and viscosity respectively, Ω is the rotational velocity, R the radius and $C_{0.75R}$ are chord length at 75% of the blade radius.

The flight regime of interest in this study is hover where the flow is treated as one dimensional. The hovering performance is evaluated by the Figure of Merit FM which is defined as the ratio of ideal power to the actual power. It is given as follows:

$$FM = \frac{P_i}{P_A} = \frac{T^{3/2}}{P\sqrt{2\rho A}} = \sqrt{\frac{2}{\pi}}\frac{C_T^{1.5}}{C_P} \quad \text{.....} \quad (2)$$

Where C_T and C_P are thrust and power coefficients respectively given by

$$C_T = \frac{T}{\rho n^2 D^4},\ C_P = \frac{P}{\rho n^2 D^5}\ and\ n = \frac{\Omega}{60}\left(\frac{revolution}{second}\right) \text{.....} \quad (3)$$

3. Numerical method

3.1. Governing Equations and Transition Model

High fidelity CFD is utilized to carry out the flow simulation over the airfoils and blades. The integration form of Navier-Stokes equations and of Energy equation are used as governing equations and are given respectively as:

$$\frac{\partial}{\partial t}\iiint_{\upsilon} \rho\, d\upsilon + \iint_{S} \rho V.dS = 0,$$

$$\frac{\partial}{\partial t}\iiint_{\upsilon} \rho V\, d\upsilon + \oiint_{S} (\rho V.dS)\, V = -\oiint_{S} p\, ds + F_{viscous},$$

$$\frac{\partial}{\partial t}\iiint_{\upsilon} \rho\left(e + \frac{V^2}{2}\right) d\upsilon + \oiint_{S} \rho\left(e + \frac{V^2}{2}\right) V.dS = \iiint_{\upsilon} \dot{q}\rho d\upsilon - \oiint_{S} pV.dS + \dot{Q}_{viscous} + \dot{W}_{viscous}. \quad \text{.....} (4)$$

Where V and p are the freestream velocity and the pressure respectively, e and $\dot{q}$ are internal energy and volumetric rate of heat addition per unit mass respectively, $F_{viscous}$ is the viscous force, $\dot{Q}_{viscous}$ and $\dot{W}_{viscous}$ are the rate of heat and work due to viscous effects respectively. The letters υ and S denote control volume and surface.

The above equations introduced more unknowns than the number of equations. Assuming that the fluid is continuous and the gas molecules are calorically perfect, the equation of state and the internal energy equation can be added to solve for the unknowns in (4) and given respectively by:

$$p = \rho RT\ and\ e = C_v T \quad \text{.....} \quad (5)$$

where T is the temperature, R and C_v are the gas constant and heat specific at constant volume respectively.

Moreover, the transition model $\gamma - \mathrm{Re}_\theta$ SST based on four transport equations is employed to discretize the governing equations into algebraic equations.

3.2. Airfoil Aerodynamic Performances

The performance of the three airfoils, to know NACA5605, Camber 4603 and DEP 4535-01 was evaluated at the radial station $r/R = 0.75$, corresponding to a chord-based Reynolds number of $Re_c = 18692$ and Mach number of $Ma = 0.56$. The static pressure and specific heat ratio were 720kPa and 1.3 respectively and the chord length of these airfoils was 90mm.

Counsil et Boulama [18] studied the effect of the computational domain on the flow features where two domains of 10c and 20c upstream of the airfoil were considered. For both configurations, the far-field downstream of the airfoil was 20c. It was found that the domain of 20c upstream the airfoil was independent of the separation and reattachment points. Thus, the current computational domain was designed after their configuration as shown in Figure 2. As the freestream Mach number exceeded 0.3, the pressure-far-field boundary condition was applied to the edges of the computational domain. Besides the effect of the computational domain, numerical results depend on the grid density. A total of 4 grids with C-H typology centered around the airfoil were considered to study the grid sensitivity at angle of attack of $\alpha = 6deg$ (see Table 1). A medium grid resolution denoted by Grid 1 was originally created. Grids 2 and 3 were generated by refining Grid 1 in the wall normal and streamwise directions respectively. And Grid 4 was obtained by equally refining Grid 3 by the factor of $\sqrt{2}$. For all the cases, the first cell distance was set as $1 \times 10^{-5}$where y^+ did not exceed 1.

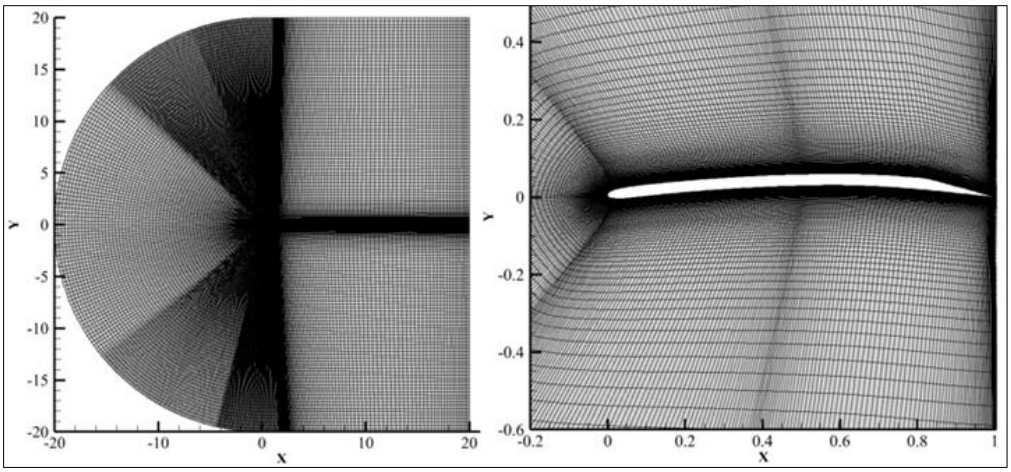

Figure 2 Computational domain and grid typology around Camber 4603 airfoil.

The computed results using $\gamma - Re_\theta\ SST$ model at $\alpha = 6deg$ were summarized in Table I. The lift and drag coefficients were taken as the average over the number of iterations. The cases 1 and 2 were inappropriate as they predict larger C_l and C_d. However, cases 3 and 4 predicted relatively consistent results. Because case 4 was generating by refining case 3 by the factor of $\sqrt{2}$, case 3 was therefore chosen for the rest of the study.

Table 1 Grid independence verification around the airfoil

Grid	Grid density	AoA, deg	C_l	C_d
1	480x135	6	1.07003	0.10331
2	480x190		1.06943	0.10315
3	630x190		1.05047	0.09960
4	886x268		1.04916	0.09956

The performance of the three airfoils defined by the ratio of the lift coefficient to drag coefficient over the angles of attack spectrum is shown in Figure 3. Two regions could be identified. From $\alpha \leq 4deg$, the airfoil performances increased suddenly and reached the peak values. The peak values of DEP 4534-01, NACA 5605 and Camber 4603 airfoils were 23, 21 and 20 respectively. The other region started after $\alpha = 4deg$ where the performance decreased due to the increase in drag component. Moreover, from $\alpha = 9deg$, DEP 4535-01 airfoil outperformed NACA 5605 and Camber 4603 airfoils. However, post $\alpha = 9deg$, its performance dropped below that of NA5605. From this result, it can be said that the airfoils with small thickness are beneficial at low angles of attack in the low Reynolds number compressible flow. Whereas at high angles of attack where the flow separation is pronounced, an airfoil with a fair thickness such as the case of NACA 5605 airfoil proved to be aerodynamically effective. These three airfoils were used further to design the blades in order to compare their 3D hovering performance.

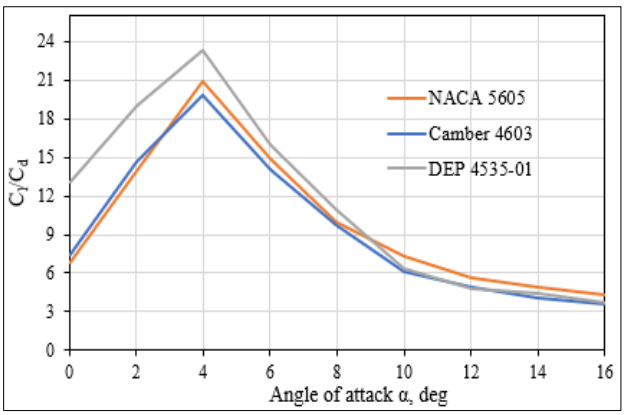

Figure 3 Aerodynamic performance of the three airfoils

3.3. Grid Sensitivity Study

CFD results depend mainly on three factors: mesh sensitivity and computational domain, turbulence model and settings. However, previous studies have proved that the mesh sensitivity made a huge impact on the result and having a good quality of the mesh with fair number of elements can minimize the computational error. Kwon et al. [19] stated that due to the complexity of propeller's geometry, the computational domain ought to be larger, from 7 to 10 blade radius in order to accurately capture the flow features of the wake vortices near the blade tip. Figure 4 shows the computational domain, a half cylinder with a radius of 10R and height of 60R. The blade was placed at 20R and 40R away from the front surface and rear surface respectively. A structured mesh is used for the entire domain and the blade. Pressure-far-field was applied to inlet and outlet boundary conditions and the rotational periodic was applied to the two parts of the bottom surface. The second order Scheme was utilized to minimize errors.

Table 2 Grid independence verification around the blade

Grid	No. of spanwise nodes	No. of chordwise nodes	No. of leading edge nodes	No. of elements
Grid 1	121	42	14	1.20×10^5
Grid 2	150	52	16	2.15×10^6
Grid 3	183	65	20	3.75×10^6
Grid 4	216	78	32	5.06×10^6

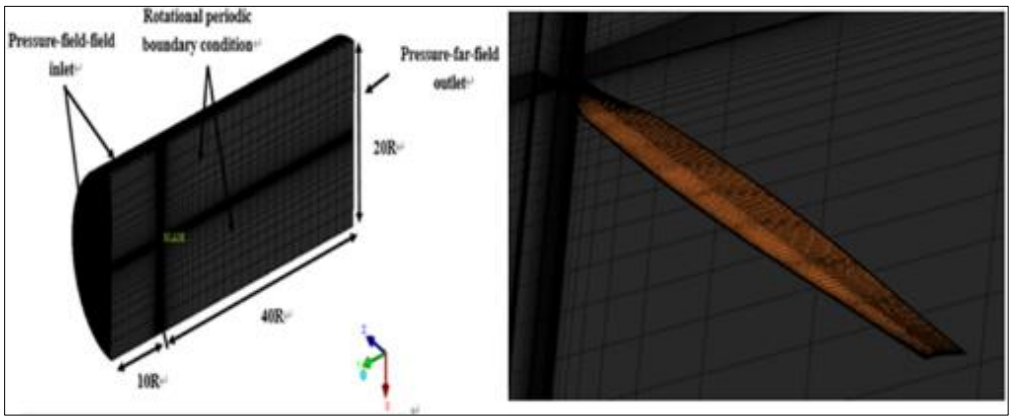

Figure 4 Computational domain and blade grid

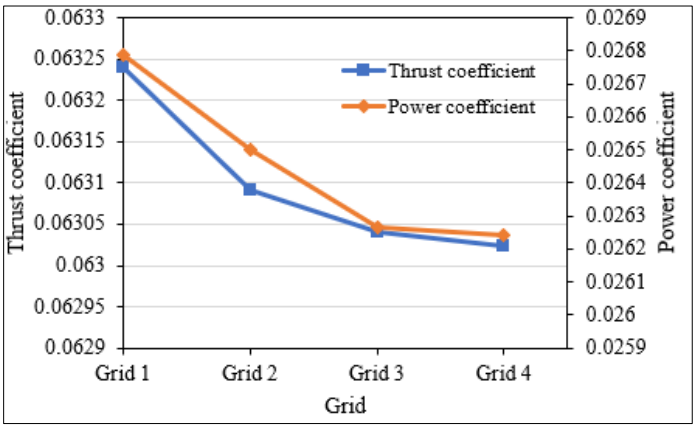

Figure 5 Thrust and power coefficient of the four grids

A number of blades were to be computed and it is crucial to find a grid density which is independent. To validate the grid independence, four grids with different densities were considered to compute for the aerodynamic characteristics where the rotational speed is 2783RPM and the incoming flow is zero. Figure 5 displays the thrust and power coefficients of the four grids. It can be noticed that as the grid density increased, the result became stable. The grids 1 and 2 were not appropriate as the results of thrust and power coefficients are not stable. Grids 3 and 4 gave a nearly stable thrust and power coefficients. The convergence criteria for Grid 3 shown in Figure 6 were below 10^{-4}. Thus, considering the computational time, the density for Grid 3 was adapted to the blades.

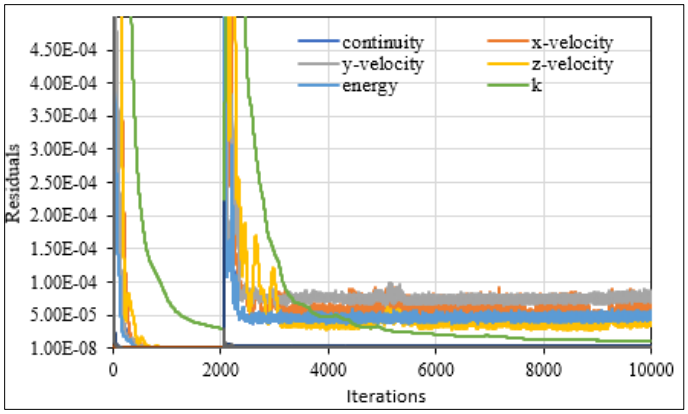

Figure 6 Plot of residuals over iterations of Grid 3

4. Results

4.1. Performance Curve

The hovering flight regime is the distinguishing feature of the rotary-wing from the fixed-wing. This flight regime is performed by generating thrust to offset the gravitational force. The gravitational acceleration on Mars is about $g = 3.72\text{m/s}^2$ resulting in the required thrust per blade of $T_{req} = 1.67\text{N}$ for a payload of $m = 1.8kg$. Figure 7 showcases the aerodynamic characteristics (thrust and torque) of the three blades at 2783RPM. At a pitch angle of 0deg, all the three blades did not generate sufficient thrust to perform hovering; thus, the performance curve was conducted with a pitch angle increment of 2deg. NACA 5605 blade met the required thrust earlier along the pitch angle than Camber 4603 and DEP 4535-01 blades. As can be seen in Fig. 7, the thrust generated by the three blades increased linearly whereas the torque parabolically with the increase in pitch angles. NACA 5605 blade generated high thrust and torque compared to the other blades due to the high camber and thickness distribution of the airfoil. The thrust generated by Camber 4603 and DEP 4535-01 were somewhat the same. Prior to pitch angle of 8deg, DEP 4535-01 generates minimum torque compared to NACA 5605 and Camber 4603 blades; however, the torque increased significantly beyond 8deg.

Figure 8 displays the Figure of Merit FM of the three blades over the pitch angle range of [0deg, 12deg]. The FM of the three blades reached its peak at pitch angle of 8deg. Prior to this pitch angle, DEP 4535-01 blade outperformed NACA 5605 and Camber 4603 blades. However, post this pitch angle, DEP 4535-01 blade performance dropped below that of NACA 5605 blade. At the peak FM pitch angle, the hovering performance of DEP 4535-01, NACA 5605 and Camber 4603 blades were 0.73, 0.71 and 0.70 respectively. It can be concluded that the type of airfoil to be used for Martian blade design depended on the pitch angle as the airfoil performance depended on the angle of attack.

DEP 4535-01 blade at pitch angle of 8deg is selected to examine the thickness distribution by conducting structural analysis.

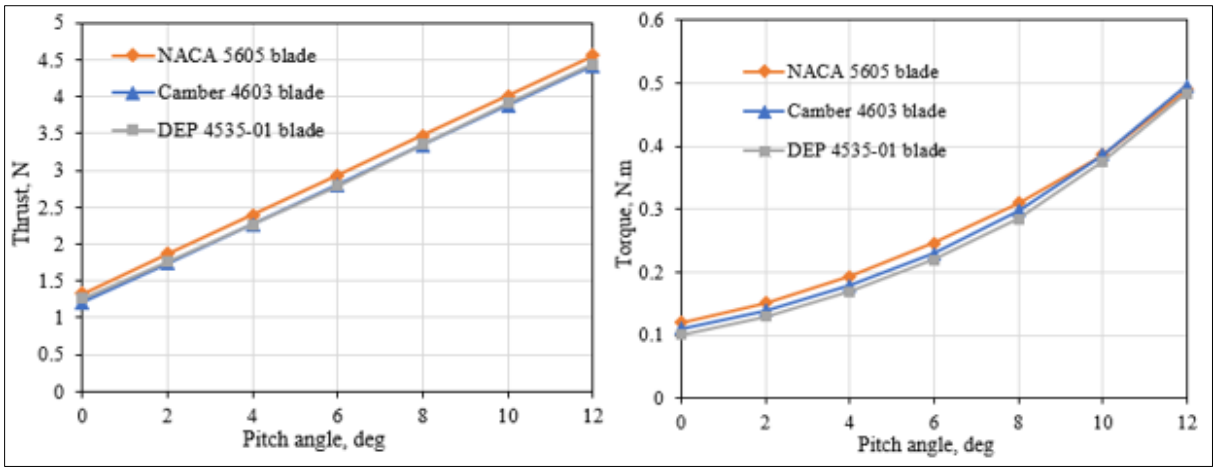

Figure 7 Aerodynamic characteristics of the three blades

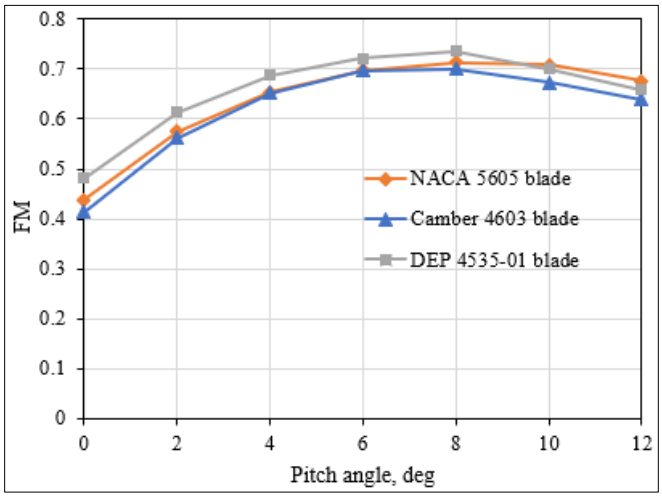

Figure 8 Figure of Merit of the three blades

4.2. Structure Analysis

Table 3 Material properties of carbon fiber

Property	**Value**
Density, kg/m^3	1850
Young Modulus E_x, 10^{11} Pa	2.3
Young Modulus E_y, 10^{11} Pa	2.3
Poisson's ratio, ν_{xy}	0.2
Shear Modulus, G_{xy}, 10^9 Pa	9

The structural analysis of the double-edged plate blade was carried out using Static Structure workbench within the commercial software Ansys. The main purpose was to assure the structural safety of the blade under external loads.

The selection of the material is based on the compatibility of the chosen material with Martian atmosphere and its weight. The Martian atmosphere is humid where the average temperature is roughly −60°C [20]. With this low temperature, materials are subject to corrosion which reduces the fatigue life. Because of its ability to resist corrosion and lightweight [21], Carbon Fiber was applied to the blade with its properties listed in Table 3. Figure 9 shows the blade structured mesh with 735672 elements and the applied loads. The blade hub was constrained as fixed boundary condition and a free boundary condition was set at the blade tip. The external loads applying on the blade were the centrifugal force due to the rotation of the blade and pressure contours obtained from Fluent solver.

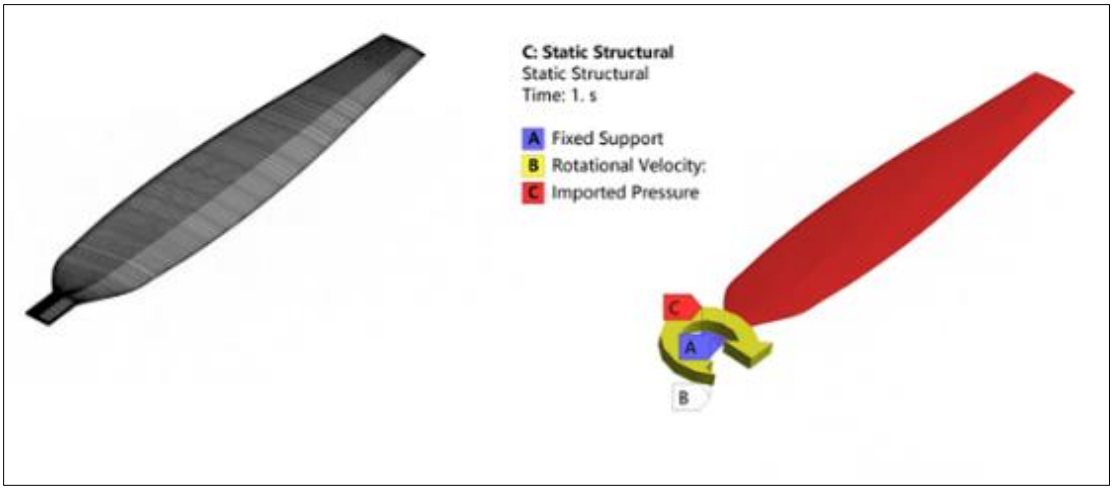

Figure 9 Blade structured mesh and loads applied on the blade

The total deformation and maximum equivalent stress are the set metrics to evaluate the structural safety of the blade. Figure 10 displays the stress and deformation of DEP 4535-01 blade at pitch angle of 8deg under the applied loads. The maximum stress occurs in the root section with a value of 393.15MPa. The tip section of the blade experiences the highest deformation of magnitude of 485.54mm. Furthermore, the factor of safety FoS defined as the ratio of the maximum stress to the working stress has a maximum value of 15 and a minimum of 1.12. This minimum value of FoS may require adding internal structures to increase the fatigue life and reduce the deformation.

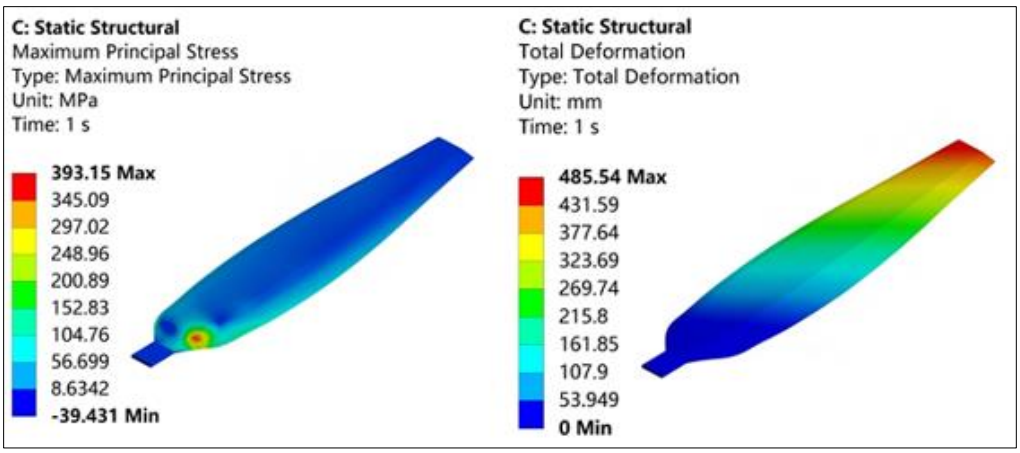

Figure 10 Stress and deformation of DEP 4535-01 blade at pitch angle of 8deg.

5. Conclusion

Martian atmosphere is characterized by low density and low speed of sound leading to a low Reynolds number compressible regime which reduces the overall performance by inducing flow separation and shock wave. The current study investigated the 2D performance of NACA 5605, Camber 4603 and DEP 4535-01 airfoils at Mach number of $Ma = 0.56$ and the chord-based Reynolds number of $Re_c = 18692$ and the 3D hovering performance of the blades at tip Mach number of $M_{tip} = 0.75$. The 2D and 3D performance curves were conducted for the angles of attack range of [0deg,

16deg] and the pitch angle range of [0deg, 12deg] respectively, with an increment of 2deg. The following conclusions could be drawn from this study:

- For the 2D performance, the result showed that the airfoil with the smallest thickness, which was DEP 4535-01 outperformed the other airfoils at low angles of attack in the low Reynolds number compressible flow. Whereas its performance dropped below that of NACA5605 at high angles of attack.
- As for the blade hovering performance, the result proved that the selection of the airfoil type depended on the peak FM pitch angle which was 8deg. Prior to the pitch angle of 8deg, DEP 4535-01 blade outperformed NACA 5605 and Camber 4603 blades. Post to that pitch angle, DEP blade performance dropped suddenly below NACA blade. At the peak FM pitch angle, the Figure of Merit of DEP 4535-01, NACA 5605 and Camber 4603 blades were 0.73, 0.71 and 0.70 respectively.

Finally, to ensure the structural safety of DEP blade, the structure analysis was conducted at a pitch angle of 8deg. The maximum stress and deformation were 393.13 MPa and 485.54mm respectively and the minimum and maximum factors of safety were 1.12 and 15 respectively, demanding internal structures for the blade.

Compliance with ethical standards

Acknowledgments

The authors would like to thank all the authors of the references used to support this work. The present work was supported by the National Natural Science Foundation of China under Grant No. 12002161, 12032011, and the National Key Laboratory of Helicopter Aeromechanics, Funding No. 2023-HA-LB-067-06

Disclosure of conflict of interest

The authors declare no conflict of interest.

References

[1] L. A. Young, Vertical lift—not just for terrestrial flight, American Helicopter Society International Powered Lift Conference, Crystal City, VA, October 2000.

[2] P. C. O'Brien, Using a robotic helicopter to fuel interest in and augment the human exploration of the planet mars, AIAA Paper No. 2993-6275, September 2003.

[3] J. Balaram, I. J. Daubar, J. Bapst, and T. Tzanetos, Helicopters on mars: compelling science of extreme terrains enabled by an aerial platform, Ninth International Conference on Mars, Pasadena, CA, July 2019.

[4] W. J. F. Koning, E. A. Romander, and W. Johnson, Low Reynolds number airfoil evaluation for the mars helicopter rotor, American Helicopter Society 74th Annual Forum, Phoenix, AZ, May 2018.

[5] W. J. F. Koning, W. Johnson, and H. F. Grip, Improved mars helicopter aerodynamic rotor model for comprehensive analyses, AIAA Journal, Vol. 57, No. 9, September 2019.

[6] W. J. F. Koning, Airfoil selection for mars rotor applications, NASA/CR—2019-220236, July 2019.

[7] T. Désert, J-M. Moschetta, and H. Bézard, Aerodynamic design of a martian micro air vehicle, 7th European Conference for Aeronautics and Aerospace Sciences (EUCASS).

[8] A. Oyama, and K. Fujii, A Study on airfoil design for future mars airplane, 44th AIAA Aerospace Sciences Meeting and Exhibit, 9-12 January 2006, Reno, Nevada.

[9] W. J. F. Koning, B. N. Perez Perez, H. V. Cummings, E. A. Romander, and W. Johnson, ELISA: A tool for optimization of rotor hover performance at low Reynolds number in the mars atmosphere, 6th Decennial Aeromechanics Specialists' Conference, Santa Clara, CA, USA Feb.6-8, 2024.

[10] P. Munday, k. Taira, T. Suwa, D. Numata, and K. Asai, Non-linear lift on a triangular airfoil in low-Reynolds-numbers compressible flow, Journal of Aircraft, Vol. 52, No. 3, 2015, pp. 924-931.

[11] B. G. Marinus, N. Mourousias, and A. Malim, Exploratory optimizations of propeller blades for a high-altitude pseudo-satellite, AIAA AVIATION 2020 Forum, June 15-19, 2020, VIRTUAL EVENT.

[12] H. H. Mian, G. Wang, H. Zhou, and X. Wu, Optimization of thin electric propeller using physics-based surrogate model with space mapping, Aerospace Science and Technology, February 2021.

[13] A. Brocklehurst, and G. N. Barakos, A review of helicopter rotor blade tip shapes, Progress in Aerospace Science 56 (2013) 35-74.

[14] W. J. F. Koning, W. Johnson, and H. F. Grip, Improved Mars helicopter aerodynamic rotor model for comprehensive analyses, AIAA Journal, Vol. 57, No. 9, September 2019.

[15] K. Lodefier, B. Merci, C. De Langhe, and E. Dick, Transition modeling with the SST turbulence model and intermittency transport equation, ASME Paper GT2003-38282, June 2003.

[16] R. B. Langtry, and F. R. Menter, Correlation-Based transition modeling for unstructured parallelized computational fluid dynamics codes, AIAA Journal, Vol. 47, No. 12, 2009, pp. 2894-2906.

[17] R. Lumba, C. Chi, A. Datta, W. Koning, N. Perez Perez, and H. Cummings, Structural design and aeromechanical analysis of unconventional blades for future mars rotorcraft, Journal of the American Helicopter Society, 2023.

[18] J. N. N. Counsil, and K. G. Boulama, Low-Reynolds-number aerodynamic performances of the NACA 0012 and Selig Donovan 7003 Airfoils, Journal of Aircraft, Vol 50, No 1, 2013.

[19] H. Il Kwon, S. Yi, S. Choi, and K. Kim, Design of efficient propellers using variable-fidelity aerodynamic analysis and multilevel optimization, Journal of Propulsion and Power, vol. 31, no. 4, July-August 2015.

[20] W. J. F. Koning, W. Johnson, and H. F. Grip, Improved mars helicopter aerodynamic rotor model for comprehensive analyses, AIAA Journal, Vol. 57, No. 9, September 2019.

[21] S.A. Mirdehghan, Fibrous polymeric composites, ScienceDirect, the Textile Institute Book Series2 021, Pages 1-58.